



Supplementary Materials for

Photonic spin-controlled multifunctional shared-aperture antenna array

Elhanan Maguid, Igor Yulevich, Dekel Veksler, Vladimir Kleiner, Mark L. Brongersma,
Erez Hasman*

*Corresponding author. Email: mehasman@technion.ac.il

Published 21 April 2016 on *Science* First Release

DOI: 10.1126/science.aaf3417

This PDF file includes:

Supplementary Text
Figs. S1 to S9
Captions for Movies S1 and S2
Full Reference List

Other Supplementary Material for this manuscript includes the following:

(available at www.sciencemag.org/cgi/content/full/science.aaf3417/DC1)

Movies S1 and S2

Supplementary Text

1. Geometric phase metasurface

The geometric phase concept is an efficient approach for achieving spin-controlled phase modulation, whereas the photon spin is associated with the intrinsic angular momentum of light (21). In general, when light passes through an anisotropic and inhomogeneous medium, intrinsic angular momentum of the incident light is coupled to the extrinsic linear or orbital momentum of the emerging beam via the spin-orbit-interaction, ushering in various optical spin-Hall effect phenomena (32). In particular, it has been shown that in metasurfaces with broken inversion symmetry, the optical spin degeneracy is removed, and the light-matter interaction is manifested by the optical Rashba effect (20, 33). The alliance between the shared-aperture and geometric phase concepts provides a route for spin-controlled multifunctional metasurfaces. The peculiarity of the geometric phase lies in its geometric nature; unlike diffractive and refractive elements, it does not arise from optical path differences but from a space-variant manipulation of the light's polarization state (16, 17). By tiling a metasurface with anisotropic nanoantennas, arranged according to an on-demand space-variant orientation profile $\theta(x,y)$, geometric phase metasurfaces (GPMs) are formed. High efficiency GPMs can be obtained by using an arrangement of subwavelength half-wave plates based on gap-plasmon resonators (GPRs) (23), or dielectric nano-antennas (10). Such a GPM transforms an incident circularly polarized light into a beam of opposite helicity, imprinted with a geometric phase $\phi_g(x,y) = 2\sigma_{\pm}\theta(x,y)$. Here, $\sigma_{\pm} = \pm 1$ denotes the polarization helicity (photon spin in \hbar units) of the incident light, corresponding to right and left circular polarizations, respectively. Consequently, for an arbitrary incident polarization state $|E_{in}\rangle$, the field emerging from a space-variant half-wave plate is given by $|E_{out}\rangle \propto \exp[i2\theta(x,y)]\langle\sigma_-|E_{in}\rangle|\sigma_+\rangle + \exp[-i2\theta(x,y)]\langle\sigma_+|E_{in}\rangle|\sigma_-\rangle$, where $|\sigma_{\pm}\rangle$ stands for the spin state, and $\langle\alpha|\beta\rangle$ denotes the inner product (17, 18).

2. Shared aperture approaches

Three approaches have been proposed for the realization of a multifunctional shared-aperture phased array: segmentation, interleaving (1-4), and harmonic response (HR) (24-26). In the segmentation approach the aperture is spatially divided into separated sub-arrays imprinted with different phase functions (Fig. 1A). As a result of such a division, the reduction of angular resolution is inevitable. To enhance the angular resolution, the interleaved approach is applied where multiple desired phase profiles are interleaved within the entire aperture (Fig. 1B). Each phase profile is associated with a different sub-array, and subjected to a thinning process – spatial sampling of fragments of a specific phase array. The thinning procedure can be implemented using several methods, e.g., combinatorial algorithm, fractal arrangement, or stochastic optimizations to achieve sufficient bandwidth, adequate signal-to-noise ratio (SNR), and desired functionality (1-4). Note, the sub-arrays are composed of a large number of fragments which can be scaled down up to a single elementary radiator. However, the stochastic thinning process affects the SNR of the radiation profile; for subwavelength fragments, the noise is attributed to speckles, while for significantly larger fragments, most of the noise ushers in side lobe level. In order to improve the SNR, an HR approach can be adopted in which

the harmonic orders of the phase function are exploited to achieve multiple wave-fronts (Fig. 1C). The channel capacity of N_c phase profiles within the shared-aperture phased array of area A can be estimated by the Gabor theory of information (34) in the absence of noise. For a given solid angle of Ω , and wavelength λ , the diffraction limit of each plane-wave (channel) reveals that for the segmentation approach $N_c \approx \sqrt{A\Omega/\lambda^2}$, whereas for the interleaving and HR approaches $N_c \approx A\Omega/\lambda^2$ (35). Consequently, the Gabor limit of the information capacity for the latter approaches is significantly higher.

3. High efficiency geometric-phase metasurface based on gap-plasmon resonance nanoantennas

High efficiency geometric phase metasurfaces (GPMs) are obtained by using an arrangement of subwavelength half-wave plates based on gap-plasmon resonators (GPRs). In order to obtain building blocks serving as half-wave plates, the performance of the GPR nanoantennas has been investigated. These GPMs are based on GPR nanoantennas that consist of metal-insulator-metal layers creating a resonator for surface-plasmon standing waves thereby enabling high reflectivity by increasing the coupling between the free-wave and the fundamental resonator mode. Moreover, adjustment of the GPR nanoantenna's dimensions enables the design of high efficiency half-wave plate (23), aimed to be as small as possible in order to achieve a high spatial sampling frequency $f = s/\lambda$, where s is number of samples per wavelength. Consequently, the metasurface is composed of a continuous SiO_2 , 110nm film sandwiched between a continuous gold substrate beneath it with gold nanobricks on top. The nanobricks, with dimensions of $210 \times 70 \times 30 \text{nm}^3$, are arranged in a square array with a lattice constant of 250nm composing the metasurface of diameter $D = 50 \mu\text{m}$. Such a structure results in $s \approx 4$ for the near-IR regime, to ensure low crosstalk between the nanoantennas (Fig. S1A). We numerically studied by use of finite-difference time-domain (FDTD) the reflection coefficients r_x, r_y and phase retardation Φ of a uniformly oriented GPR nanoantenna array (Fig. S1B), illuminated with two orthogonal linear polarizations, providing the values of $r_x \approx 0.9$; $r_y \approx 0.97$, and $\Phi \approx \pi$ for a broadband spectrum operation of $\lambda \sim 700\text{-}1000\text{nm}$ (Fig. S1, D and E), which are in good agreement with the experimental results. The obtained parameters usher in a diffraction efficiency for a

blazed GPM of $\sim 90\%$ (Fig. S1F) according to $\eta_{\sigma_{\pm}} = \left| \frac{1}{2} (r_x - r_y e^{i\Phi}) \langle \sigma_{\mp} | E_{in} \rangle \right|^2$, in agreement with the FDTD simulation, where the experimental efficiency was found to be $\sim 79\%$ (Fig. S1C, F and G). The diffraction efficiency was calculated as a ratio between the intensity of a specific channel and the incident illumination intensity.

Moreover, wave-front frequency multiplexing within a shared-aperture GPM requires the design of narrowband nanoantennas. For this purpose, we simulated two GPR nanoantennas, which consisted of a pair of gold nanobricks (Fig. S1H). Such configurations provide distinguishable phase-retardation resonances at wavelengths of 770nm and 1000nm (Fig. S1, D and E), and diffraction efficiencies of $\sim 70\%$ (Fig. S1F).

4. FDTD simulation of multiple wavefronts generated by interleaved GPM

We performed an FDTD simulation of the interleaved GPM (Fig. 2A) and observed 3x2 spin-controlled OAM wavefronts with the desired topological charge of $0, \pm 1, \pm 2$ (Fig. S2), in agreement with the experimental result provided in the main text (Fig. 2, B and C).

5. Achromatic nature of geometrical phase

Geometric phase metasurfaces based on GPR nanoantennas can operate within a broad wavelength range. Unlike diffractive and refractive elements, the peculiarity of the GPMs lies in their geometric nature, in which the phase-pickup does not arise from optical path differences but from a space-variant manipulation of the light polarization state. The geometric phase of $2\sigma_{\pm}\theta(x, y)$ generated by space-variant anisotropic nanoantennas depends only on the incident circular polarization and on the local orientation angle $\theta(x, y)$ of the nanoantennas, hence, the geometric phase is wavelength independent. We experimentally studied the achromatic nature of the geometric phase by illuminating the interleaved GPM (Fig. 2A) at several operating wavelengths (Fig. S3), and observed the same annular patterns, indicating the achromatic spiral phase-fronts.

6. Calculation of Far-field intensity distributions for interleaved metasurface

In order to estimate the impact of an incrementally growing number of wave-fronts on SNR, the far-field intensity distributions were calculated via Fourier transform yielding

$$\left| \sum_j^N \sum_v^{n_j} \exp \left\{ ikr_v^{(j)} + i\phi_g \left(r_v^{(j)} \right) \right\} \right|^2, \text{ where } r_v^{(j)} \text{ are the positions of } v \text{ nanoantennas, and } \phi_g \left(r_v^{(j)} \right) \text{ stands for the geometric phase of } j\text{-th sub-array.}$$

7. Angular resolution comparison between segmented and interleaved GPMs

We experimentally examined the angular resolution of segmented and interleaved GPMs generating four and nine independent channels (plane waves). It can be seen from Fig. S4 that the spot size obtained by the interleaved GPM remains the same under the increasing number of generated channels, in contrast to the segmented GPM, where the spot sizes are broadened.

Moreover, we investigated the angular width of a beam emerging from the interleaved and segmented GPMs, composed of fragments with different extents. In particular, we examined a $50 \times 50 \mu\text{m}$ GPM consisting of four channels, and observed that the segmentation approach (Fig. S5A) leads to a larger angular width with respect to a GPM of a single channel (see Fig. S5E). Further gradual reduction of the fragment's size (Fig. S5B) as required for the interleaving procedure, results in increasing side lobes. A significant reduction of the fragment's size leading to a small side-lobe level, however, is accompanied by speckle noise originating from the interleaving procedure (Fig. S5E).

8. Generation of multiple vectorial vortices

An additional peculiar twist in the field of metasurfaces relies on space-variant polarization manipulation, which may encompass a broader class of wave-front shaping. Formation of multifunctional vectorial vortices is of great interest for optical communications, fiber mode shaping (36), super-resolution (37), optical tweezers, tractor beam (38) and laser beam shaping (39). Interleaved GPM enables obtaining multiple vectorial vortices by coherent superposition of wave-fronts with opposite helicities. When illuminating the GPM with linearly polarized light, the emerging field consists of two opposite circularly polarized states (18, 19). In particular, for a geometric phase profile of the form $\phi_g(x, y) = \sigma_{\pm} l \varphi$ these states carry conjugate scalar vortices with winding numbers of $\sigma_{\pm} l$. Superposition of in-phase and π -phase shifted conjugated scalar vortices of $l=1$ with opposite spin states results in radial and azimuthal polarization, respectively (Fig. S6A). We utilized the interleaving approach in order to realize a GPM with two phase functions $\phi_g^{(1)}(x, y) = \sigma_{\pm} [\text{U}_{\pi}(\cos(k_x x)) + \varphi]$ (in-phased), and, $\phi_g^{(2)}(x, y) = \sigma_{\pm} [\text{U}_{\pi}(\cos(k_y y)) + \varphi + \pi/2]$ (π -phased), where a step function $\text{U}_{\pi}(\xi) = \{\pi, \text{when } \xi > 0; 0 \text{ otherwise}\}$ provides two main spatially separated diffraction orders with 40.5% efficiency per order. By illuminating such a GPM with linearly polarized light at a wavelength of 760nm, two radially and two azimuthally polarized beams were observed (Fig. S6B). Verification of the polarization state of the emerged beams is established by projecting these vectorial vortices on a linear polarizer (Fig. S6, C and D). Generation of scalar vortex beams is obtained by illuminating the interleaved GPM (Fig. S6A) with circularly polarized light (Fig. S6E). Verification of the circular polarization state of the emerged beams is established by projecting these scalar vortices on linear polarizers (Fig. S6, F and G). Moreover, we obtained two vectorial vortex beams with the winding number $l=2$ by orienting the nanoantennas according to $2\theta(x, y) = \text{U}_{\pi}(\cos(k_x x)) + 2\varphi$ and illuminating with linearly polarized light at a wavelength of 760nm (Fig. S6H). Verification of the polarization state of the emerged beams is established by projecting these vectorial vortices on linear polarizers (Fig. S6, I and J). The interleaved metasurfaces open up the consideration of different thinning methods for various functionalities, such as multi-frequency bands utilizing narrow-band nanoantennas (40).

9. Spin-controlled asymmetric harmonic response approach

In general, the geometric phase function can be expanded into m harmonic orders of phase function $G(\Psi)$ according to $\exp[i\phi_g(x, y)] = \exp[i\sigma_{\pm} G(\Psi)] = \sum_m A_m \exp[im\sigma_{\pm} \Psi]$. Specifically, three asymmetric harmonic orders $m \in \{1, 2, 3\}$ are obtained when an optimized analytic solution $G(\Psi) = \tan^{-1}(\mu \cos(\Psi)) + 2\Psi$ is utilized, where $\mu = 2.65718$ (25). In order to generate spin-controlled OAM harmonic orders of $l_{\pm} = \sigma_{\pm}, 2\sigma_{\pm}, 3\sigma_{\pm}$ (Fig. 3), we implemented the function $\Psi = kx + \varphi$. Moreover by setting $\Psi = kx$, we experimentally obtained spin-controlled asymmetric harmonic orders of plane-waves (Fig. S7, A and B), while by

setting $\Psi = kx + \varphi$ and $G(\Psi) = \tan^{-1}(\mu \cos(\Psi)) + 2\Psi - \varphi$, we observed three OAM harmonic response orders of $l_{\pm} = 0, \sigma_{\pm}, 2\sigma_{\pm}$ (Fig. S7, C and D). By choosing $\Psi = kx$ and $m \in \{-2, -1, 0, 1, 2\}$, we demonstrate five polarization independent harmonic orders of plane-waves (Fig. S7, E and F), while applying $\Psi = kx + \varphi$, we observed five OAM harmonic response orders of $l_{\pm} = m$ (Fig. S7, G and H).

The angular resolution (Fig. 2F) and intensity scaling of $1/N$ (Fig. 3J) were evaluated from measurements presented in figures S7B and S7F. The efficiencies of each order in figures S7B and S7F were measured to be $|A_m|^2 \cong 0.21$ and $|A_m|^2 \cong 0.104$ with uniformity of ± 0.01 and ± 0.015 , respectively. Thus, the correspondent total diffraction order efficiency provided with the values of $\sim 63\%$ and $\sim 52\%$, while the theoretical values are $\sim 92\%$ (25) and $\sim 79\%$ (24), respectively. The theoretical values multiplied by the efficiency of the GPM based on GPR nanoantennas are in agreement with the experimental result, $\sim 73\%$ and 63% respectively.

10. Information capacity analysis : Wigner phase-space and Shannon entropy

The reported spin-controlled multifunctional metasurfaces based on shared aperture approaches can be interpreted in terms of information capacity by means of Wigner phase-space distribution (41) to establish a link between the Shannon entropy and the capacity of photonic system (42, 43). The Wigner function is widely used among a variety of physical systems to represent the joint position-momentum (x - p) distribution. When the system is provided with additional spin degree of freedom, the spin-dependent Wigner function takes the form $W_{\sigma_{\pm}}^N(x, p) = \int \psi_{\sigma_{\pm}}^N(x + \xi) \{\psi_{\sigma_{\pm}}^N(x - \xi)\}^* e^{2i\xi p} d\xi$, where for GPMs $\psi_{\sigma_{\pm}}^N = \exp(-i\phi_g^N(x))$ is the field distribution function of N channels for σ_{\pm} . In order to analyze the angular resolution and intensity scaling of the channels, opened via the different shared-aperture approaches, we calculated the Wigner distribution for a spin-dependent optical field emerging from 1D multifunctional GPMs (Fig. S8, A to F). The obtained phase-space representation and corresponding momentum density $\pi_{\sigma_{\pm}}^N(p) = \int W_{\sigma_{\pm}}^N(x, p) dx$ reveals the high angular resolution of the interleaved (Fig. S8, B, E and H) and HR (Fig. S8, C, F and I) structures compared to the segmentation approach (Fig. S8, A, D and G), as expected (Fig. 2F). Yet, the intensity scaling, obtained by the integration over the momentum density (Fig. S8, G to I) is in good agreement with the analysis depicted in Fig. 2H. It is clearly seen from Fig. S8, B, E and H, that the interleaving approach is accompanied by noise, which is attributed to the speckles, resulting in a reduction of the intensity in each channel. Furthermore, we estimate the channel capacity (43, 44) of GPMs (i.e., a number of distinct channels that can be opened) utilizing spin-dependent mutual information $I_{\sigma_{\pm}}^N(X, P) = \int W_{\sigma_{\pm}}^N(x, p) \log_2 \{W_{\sigma_{\pm}}^N(x, p) / [\rho_{\sigma_{\pm}}^N(x) \pi_{\sigma_{\pm}}^N(p)]\} dp dx$ in units of bits, where $\rho_{\sigma_{\pm}}^N(x) = \int W_{\sigma_{\pm}}^N(x, p) dp$ is the position density. Figure 6J presents a numerical calculation of the $I_{\sigma_{\pm}}^N(X, P)$ for each of the GPMs. Calculation of the spin-conjugated $I_{\sigma_{\mp}}^N(X, P)$ provides a similar result. Then, the apparent limit in which one channel encoded with one

bit (Fig. S8G, dashed line) defines the available number of distinct channels N_c that can be opened. Accordingly, the channel capacity of the interleaved GPM constitutes an intermediate case between the high capacity of HR-GPM and the low capacity for the segmented GPM. It can be seen from the insets of Fig. S8J that the mutual information for $N = 7$ of HR and for $N = 8$ of interleaved GPMs is above the dashed line, leading to well resolved channels, in contrast to the segmented GPM for $N = 8$ where the channels are barely distinguishable. Note, the number of distinguishable channels according to Gabor and mutual information considerations is different, as the latter takes into account the influence of noise and spatial sampling frequency $f = s / \lambda$, where s is number of samples per wavelength, thus providing a more accurate tool for the practical design of multifunctional GPMs. In light of the above, we evaluated the number of channels $N_c \approx (\pi D / \lambda)^{\beta(s)}$ for the interleaving and segmentation approaches at different spatial sampling frequencies (Fig. S8K). Two regimes $0 \leq \beta < 1/2$ and $1/2 \leq \beta < 1$ are available to obtain distinguishable channels, where $\beta = 1/2$ and $\beta = 1$ are the Gabor limits for the segmentation and interleaving approaches, respectively. According to this analysis one can obtain a higher number of channels by increasing the sampling rate or by enlarging the extent of the metasurface.

11. Spectropolarimeter

Polarization measurement of predetermined polarization states – we illuminated the spectropolarimeter with predetermined polarization beams at a wavelength of 760nm for calibration measurement. The far field intensities of the predetermined polarization states were captured on a CCD for further analysis of their Stokes parameters (Fig. S9).

Optically active analyte – in order to demonstrate the spectropolarimetric capabilities of the proposed device, organic compounds of D- and L-glucose types were studied by measuring their specific rotation $[\alpha]_{\lambda}^T = \mathcal{G} / \ell c$. For a temperature T and wavelength λ this property is defined as the change in the orientation of linearly polarized light \mathcal{G} (deg) as it passes through a sample of $\ell = 10\text{cm}$ with a concentration of $c = 1\text{g} / \text{mL}$.

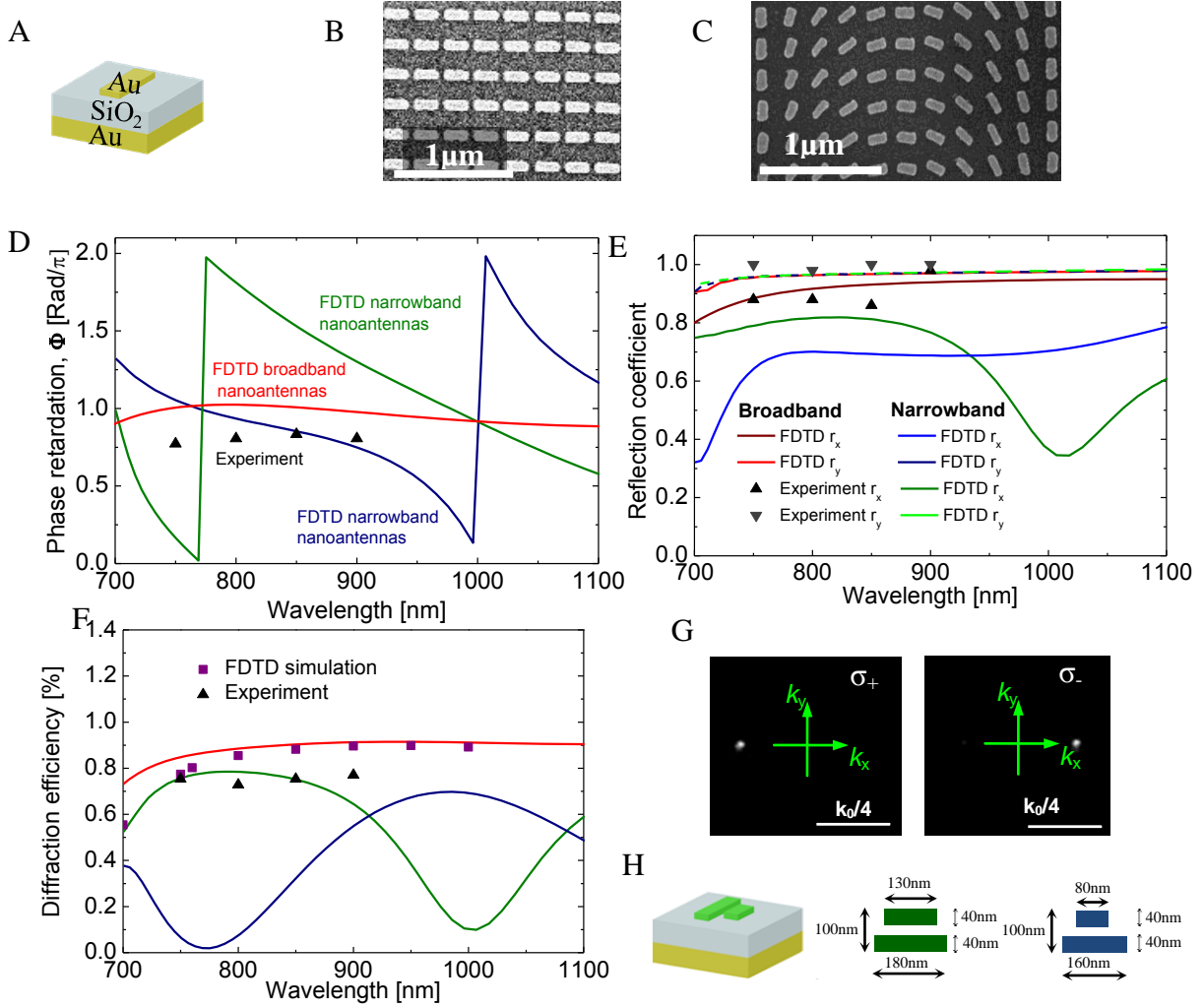


Fig. S1. Experiments and simulations of a GPR metasurface. (A) Schematic of the broadband GPR nanoantenna configuration. (B) SEM image of the uniformly oriented GPR nanoantenna array. (C) SEM image of the blazed GPM. (D) The phase retardation of the broadband and narrowband GPR nanoantennas, where the red curve and black triangles depict the simulated and experimental values for the broadband nanoantennas, while the blue and green curves depict the simulated phase retardation for the narrowband GPR nanoantennas, shown in H. (E) FDTD simulation and experimental results for the correspondent reflection coefficients. (F) Calculation and experimental results of the correspondent diffraction efficiencies for the blazed GPM shown in (C), where the purple squares assigned to the FDTD simulation. (G) Measured far-field intensity distributions of the blazed grating GPM for σ_+ and σ_- at a wavelength of 760nm. (H) Schematic of the narrowband GPR nanoantenna configuration consisting of two types of gold nanobrick pairs (green and blue, top view).

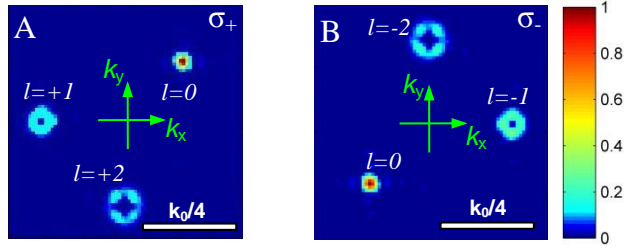


Fig. S2. FDTD simulation of multiple wavefronts generated by interleaved GPM. (A and B) Simulated spin-flip momentum deviation of three wavefronts with different OAMs at a wavelength of 760nm; σ_{\pm} denotes the incident spin.

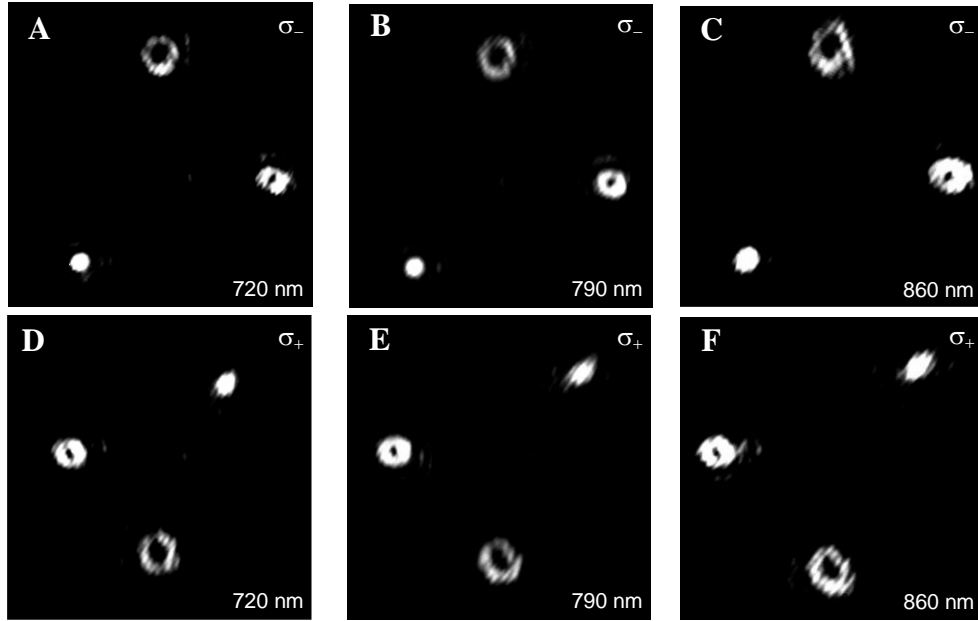


Fig. S3. Achromatic nature of geometrical phase. (A to F) Measured spin-flip momentum deviation of three wave-fronts with different OAMs at wavelengths of 720nm (A and D), 790nm (B and E), and 860nm (C and F); σ_{\pm} denotes the incident spin.

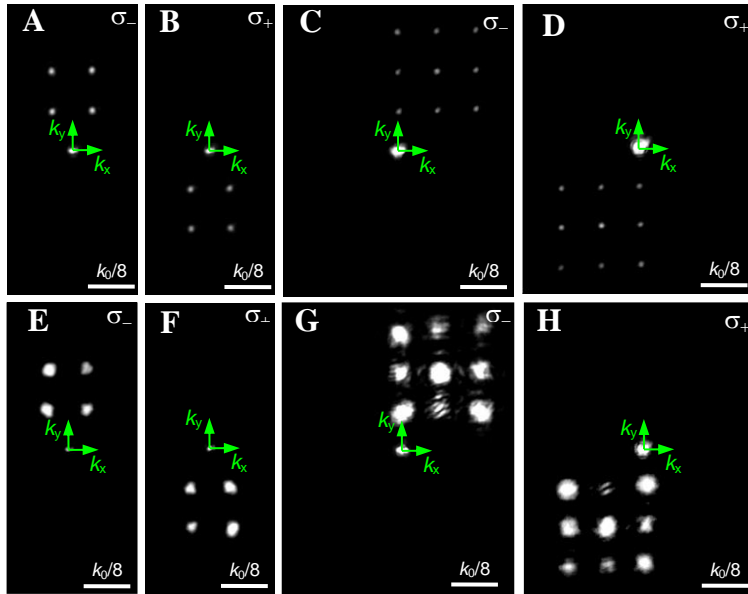


Fig. S4. Generation of multiple channels by interleaved and segmented GPMs. (A to D), Momentum deviations for the interleaved GPM of four (A and B) and nine (C and D) channels, illuminated at a wavelength of 650nm. (E to H) Momentum deviations for the segmented GPM of four (E and F) and nine (G and H) channels.

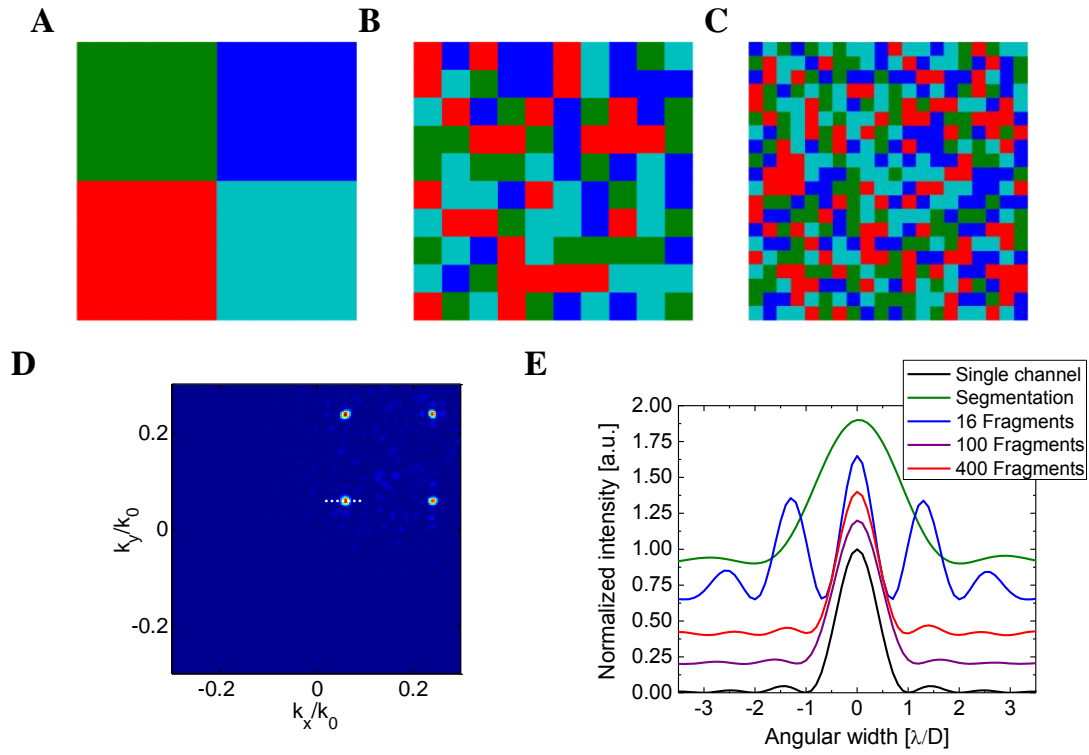


Fig. S5. Angular resolution of fragmented GPMs generating four channels. (A to C) Illustration of the GPM's fragmentation into 4 fragments by segmentation approach (A), as well as into 100 (B) and 400 (C) interleaved fragments, whereas each color represents different linear phase function. (D) The momentum space of a GPM consisting of 400 interleaved fragments. (E) Intensity distributions along the dashed white line (shown in D) of a specific channel in the momentum space for a GPM of different fragmentations.

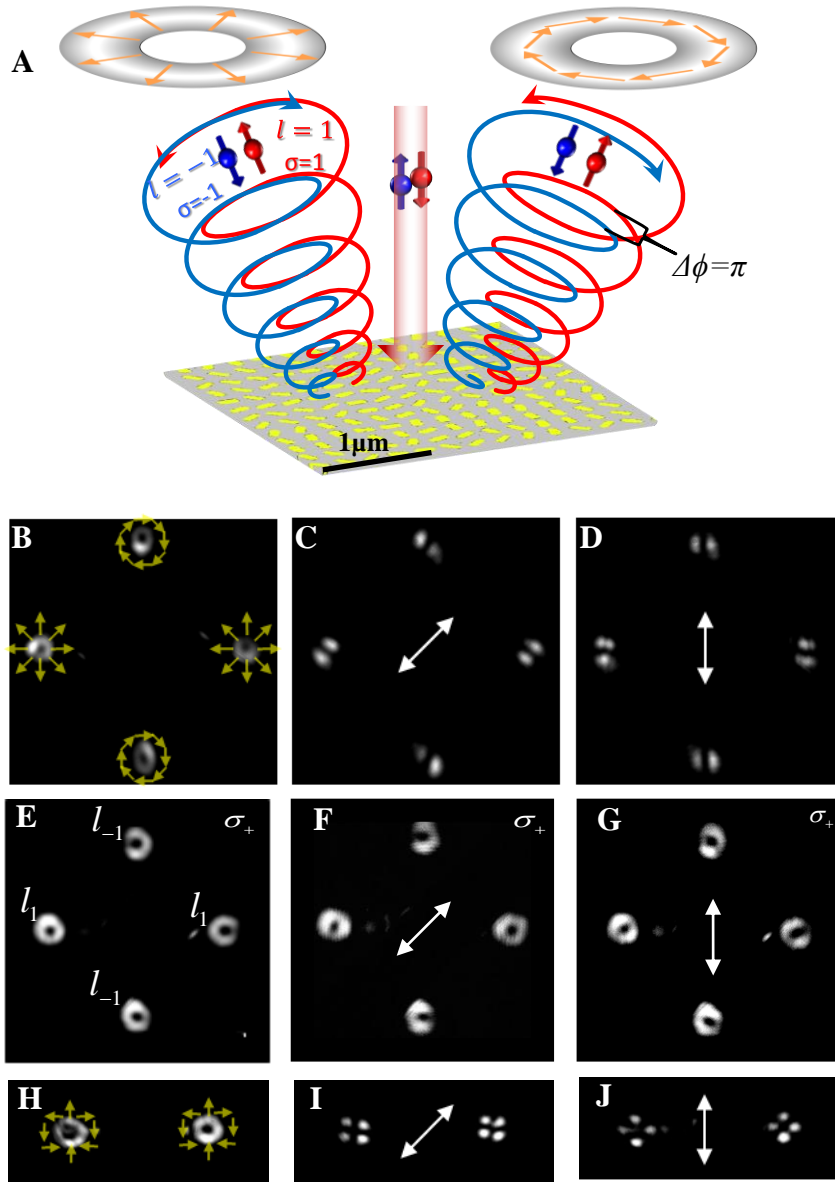


Fig. S6. Vectorial vortex beams generated by interleaved GPM. (A) Schematic of azimuthally and radially polarized beams emerging from GPM illuminated with linear polarization; red and blue helices represent scalar vortices of opposite helicities and OAMs. SEM image of the vectorial vortex interleaved GPM is presented. (B) Measured vectorial vortices, two radial and two azimuthal polarizations generated by GPM; yellow arrows represent the linear polarization distributions. (C and D) Polarization analysis of the beams wherein white arrows represent the orientation of linear polarizer-analyzer which is 45° and 0° , respectively, verifying the vectorial vortices' polarization distributions. (E to G) Observed diffraction patterns of GPM under illumination with σ_+ polarized light at a wavelength of 760nm. (F and G) Polarization analysis of the obtained

beams; arrows represent linear polarizer orientations at (I) 45° and (J) 0° . **(H)** Observed diffraction from GPM generating two vectorial vortex beams with winding numbers $l = \pm 2$, under linear polarized light illumination, at a wavelength of 760nm. **(I and J)** Polarization analysis of the beams; arrows represent linear polarizer orientations at (I) 45° and (J) 0° .

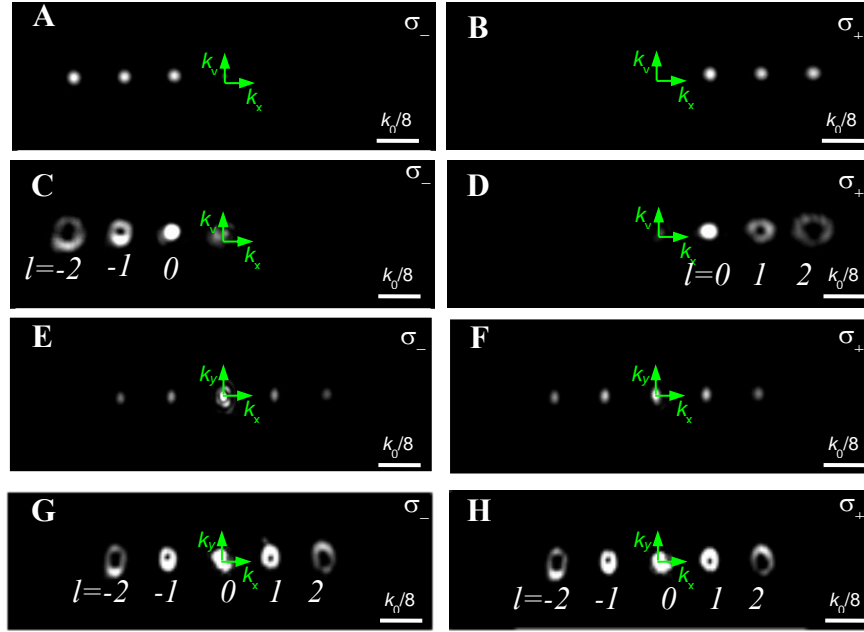


Fig. S7. Spin-controlled asymmetric harmonic response. (A to D) Measured spin-controlled HR diffractions of plane-waves (A and B) and of OAM orders (C and D), for right (σ_+) and left (σ_-) circular polarization illuminations, respectively. (E and H) Measured spin-independent five HR diffractions of plane-waves (E and F) and of OAM orders (G and H).

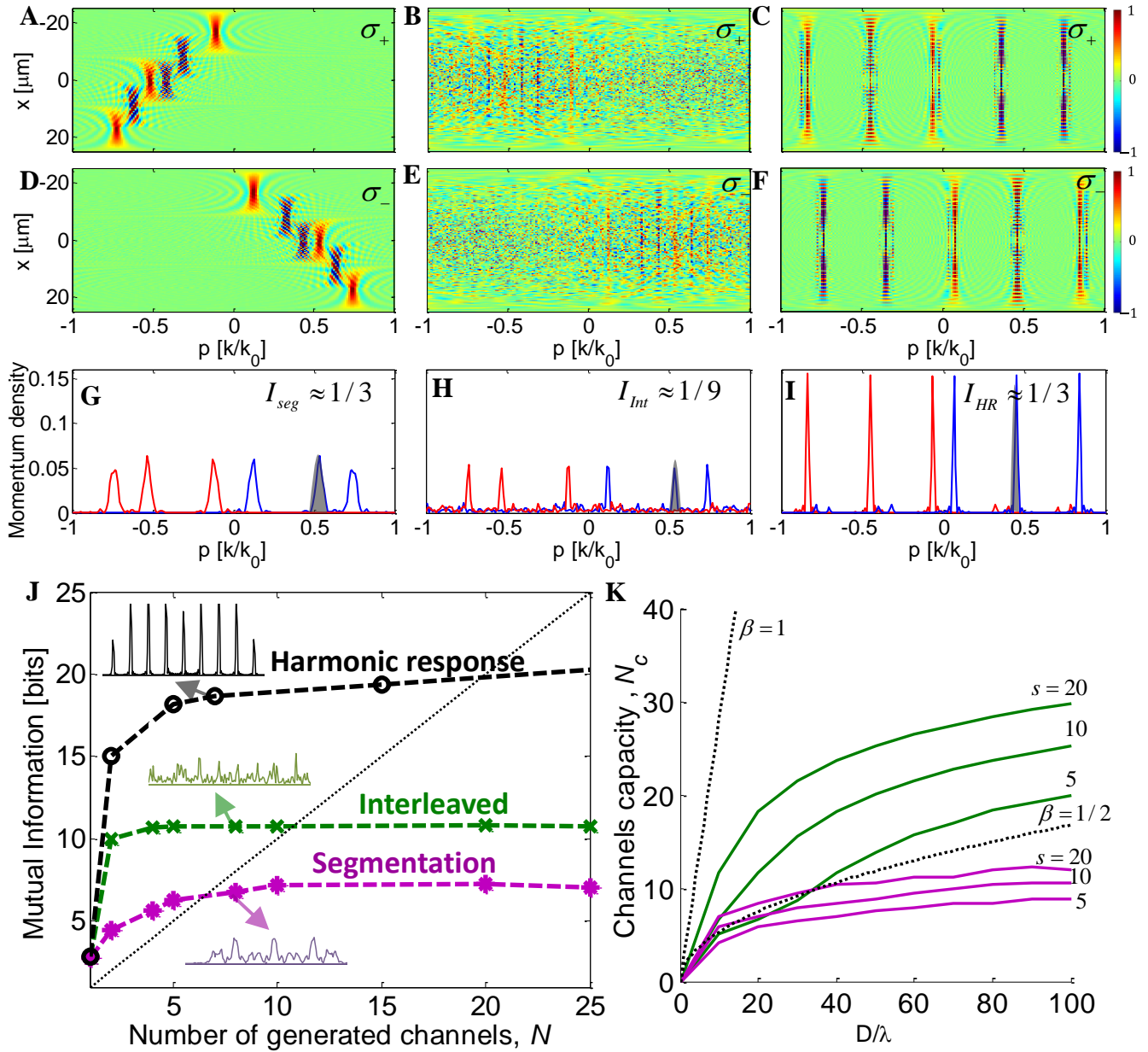


Figure S8. Wigner distributions and channel capacity of GPMs. (A to I) Calculation for a normalized aperture of $D/\lambda=50$ and $s=5$, of the spin-dependent Wigner distributions of segmentation (A and D), interleaved (B and E) and harmonic response (C and F) approaches for three channels, and their corresponding red and blue momentum densities (G to I), for σ_+ and σ_- , respectively; the shaded area denotes the intensity per channel. (J) Calculation of mutual information, the insets depict the momentum

densities of 8 channels for the segmentation (purple) and interleaved (green) GPMs, and 7 channels for the HR-GPM (black). The dashed line depicts the limit for distinguishably opened channels. (**K**) Channel capacity calculation for the segmented (purple) and interleaved (green) GPMs of different sampling (s), where the dash lines of $\beta = 1/2$ and $\beta = 1$ are the Gabor limits for the segmentation and interleaved approaches, respectively.

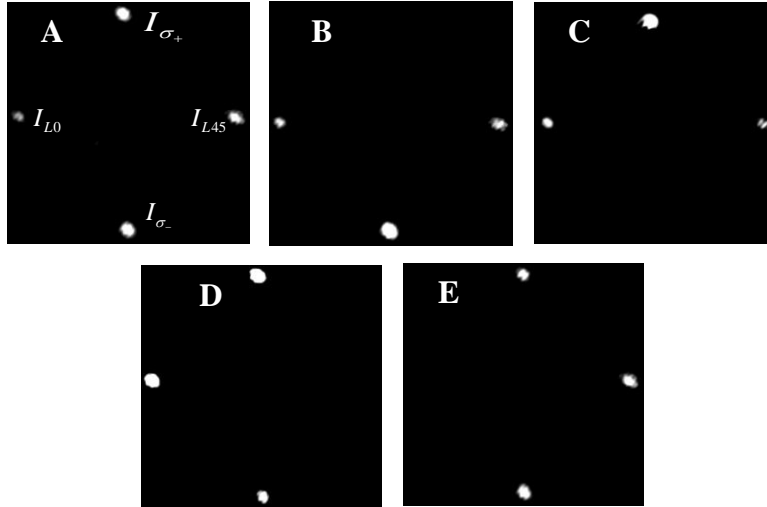


Fig. S9. Polarization measurement of predetermined polarizations. (A to E), Four channel measurements of elliptical (A), right circular (B), left circular (C), linear at 0° (D), and linear at 45° (E) polarization of light beam.

Movie S1

Vectorial vortex beams generated by interleaved GPM.

Numerical modelling for determination of polarization state of the diffracted multiple (two radial and two azimuthal polarizations) vectorial vortex beams. The calculation of the diffraction pattern obtained from the GPM shown in Fig. S6A for incident linear polarization state. This supplementary video (Movie S1) shows the changes in the diffraction pattern when rotating the polarizer-analyzer angle over 360° .

Movie S2

Vectorial vortex beams generated by interleaved GPM.

Numerical modelling for determination of polarization state of the two vectorial vortex beams with winding numbers $l = \pm 2$ presented in Fig. S6H. The calculation of the diffraction pattern obtained from an interleaved GPM for incident linear polarization state. This supplementary video (Movie S2) shows the changes in the diffraction pattern when rotating the polarizer-analyzer angle over 360° .

References and Notes

1. D. M. Pozar, S. D. Targonski, A shared-aperture dual-band dual-polarized microstrip array. *IEEE Trans. Antenn. Propag.* **49**, 150–157 (2001). [doi:10.1109/8.914255](https://doi.org/10.1109/8.914255)
2. R. L. Haupt, Interleaved thinned linear arrays. *IEEE Trans. Antenn. Propag.* **53**, 2858–2864 (2005). [doi:10.1109/TAP.2005.854522](https://doi.org/10.1109/TAP.2005.854522)
3. A. M. Sayeed, V. Raghavan, Maximizing MIMO capacity in sparse multipath with reconfigurable antenna arrays. *IEEE J. Sel. Top. Signal Process.* **1**, 156–166 (2007). [doi:10.1109/JSTSP.2007.897057](https://doi.org/10.1109/JSTSP.2007.897057)
4. I. E. Lager, C. Trampuz, M. Simeoni, L. P. Ligthart, Interleaved array antennas for FMCW radar applications. *IEEE Trans. Antenn. Propag.* **57**, 2486–2490 (2009). [doi:10.1109/TAP.2009.2024573](https://doi.org/10.1109/TAP.2009.2024573)
5. A. Papakostas, A. Potts, D. M. Bagnall, S. L. Prosvirnin, H. J. Coles, N. I. Zheludev, Optical manifestations of planar chirality. *Phys. Rev. Lett.* **90**, 107404 (2003). [Medline](https://pubmed.ncbi.nlm.nih.gov/1231758/) [doi:10.1103/PhysRevLett.90.107404](https://doi.org/10.1103/PhysRevLett.90.107404)
6. X. Yin, Z. Ye, J. Rho, Y. Wang, X. Zhang, Photonic spin Hall effect at metasurfaces. *Science* **339**, 1405–1407 (2013). [Medline](https://pubmed.ncbi.nlm.nih.gov/231758/) [doi:10.1126/science.1231758](https://doi.org/10.1126/science.1231758)
7. A. Pors, O. Albrektsen, I. P. Radko, S. I. Bozhevolnyi, Gap plasmon-based metasurfaces for total control of reflected light. *Sci. Rep.* **3**, 2155 (2013). [Medline](https://pubmed.ncbi.nlm.nih.gov/25155/) [doi:10.1038/srep02155](https://doi.org/10.1038/srep02155)
8. A. V. Kildishev, A. Boltasseva, V. M. Shalaev, Planar photonics with metasurfaces. *Science* **339**, 1232009 (2013). [Medline](https://pubmed.ncbi.nlm.nih.gov/232009/) [doi:10.1126/science.1232009](https://doi.org/10.1126/science.1232009)
9. N. Yu, F. Capasso, Flat optics with designer metasurfaces. *Nat. Mater.* **13**, 139–150 (2014). [Medline](https://pubmed.ncbi.nlm.nih.gov/23839/) [doi:10.1038/nmat3839](https://doi.org/10.1038/nmat3839)
10. D. Lin, P. Fan, E. Hasman, M. L. Brongersma, Dielectric gradient metasurface optical elements. *Science* **345**, 298–302 (2014). [Medline](https://pubmed.ncbi.nlm.nih.gov/253213/) [doi:10.1126/science.1253213](https://doi.org/10.1126/science.1253213)
11. M. G. Nielsen, D. K. Gramotnev, A. Pors, O. Albrektsen, S. I. Bozhevolnyi, Continuous layer gap plasmon resonators. *Opt. Express* **19**, 19310–19322 (2011). [Medline](https://pubmed.ncbi.nlm.nih.gov/219310/) [doi:10.1364/OE.19.019310](https://doi.org/10.1364/OE.19.019310)
12. D. Dregely, K. Lindfors, M. Lippitz, N. Engheta, M. Totzeck, H. Giessen, Imaging and steering an optical wireless nanoantenna link. *Nat. Commun.* **5**, 4354 (2014). [Medline](https://pubmed.ncbi.nlm.nih.gov/25354/) [doi:10.1038/ncomms5354](https://doi.org/10.1038/ncomms5354)
13. J. Sun, X. Wang, T. Xu, Z. A. Kudyshev, A. N. Cartwright, N. M. Litchinitser, Spinning light on the nanoscale. *Nano Lett.* **14**, 2726–2729 (2014). [Medline](https://pubmed.ncbi.nlm.nih.gov/250658n/) [doi:10.1021/nl500658n](https://doi.org/10.1021/nl500658n)
14. H.-S. Ee, J.-H. Kang, M. L. Brongersma, M.-K. Seo, Shape-dependent light scattering properties of subwavelength silicon nanoblocks. *Nano Lett.* **15**, 1759–1765 (2015). [Medline](https://pubmed.ncbi.nlm.nih.gov/254442v/) [doi:10.1021/nl504442v](https://doi.org/10.1021/nl504442v)
15. K. E. Chong, I. Staude, A. James, J. Dominguez, S. Liu, S. Campione, G. S. Subramania, T. S. Luk, M. Decker, D. N. Neshev, I. Brener, Y. S. Kivshar, Polarization-independent silicon metadevices for efficient optical wavefront control. *Nano Lett.* **15**, 5369–5374 (2015). [Medline](https://pubmed.ncbi.nlm.nih.gov/2501752/) [doi:10.1021/acs.nanolett.5b01752](https://doi.org/10.1021/acs.nanolett.5b01752)

16. Z. Bomzon, V. Kleiner, E. Hasman, Pancharatnam-Berry phase in space-variant polarization-state manipulations with subwavelength gratings. *Opt. Lett.* **26**, 1424–1426 (2001). [Medline doi:10.1364/OL.26.001424](#)
17. Z. Bomzon, G. Biener, V. Kleiner, E. Hasman, Space-variant Pancharatnam-Berry phase optical elements with computer-generated subwavelength gratings. *Opt. Lett.* **27**, 1141–1143 (2002). [Medline doi:10.1364/OL.27.001141](#)
18. G. Biener, A. Niv, V. Kleiner, E. Hasman, Formation of helical beams by use of Pancharatnam-Berry phase optical elements. *Opt. Lett.* **27**, 1875–1877 (2002). [Medline doi:10.1364/OL.27.001875](#)
19. A. Niv, G. Biener, V. Kleiner, E. Hasman, Manipulation of the Pancharatnam phase in vectorial vortices. *Opt. Express* **14**, 4208–4220 (2006). [Medline doi:10.1364/OE.14.004208](#)
20. N. Dahan, Y. Gorodetski, K. Frischwasser, V. Kleiner, E. Hasman, Geometric doppler effect: Spin-split dispersion of thermal radiation. *Phys. Rev. Lett.* **105**, 136402 (2010). [Medline doi:10.1103/PhysRevLett.105.136402](#)
21. K. Y. Bliokh, F. J. Rodríguez-Fortuño, F. Nori, A. V. Zayats, Spin–orbit interactions of light. *Nat. Photonics* **9**, 796–808 (2015). [doi:10.1038/nphoton.2015.201](#)
22. Full details can be found in the supplementary materials on *Science Online*.
23. A. Pors, M. G. Nielsen, S. I. Bozhevolnyi, Broadband plasmonic half-wave plates in reflection. *Opt. Lett.* **38**, 513–515 (2013). [Medline doi:10.1364/OL.38.000513](#)
24. H. Dammann, K. Görtler, High-efficiency in-line multiple imaging by means of multiple phase holograms. *Opt. Commun.* **3**, 312–315 (1971). [doi:10.1016/0030-4018\(71\)90095-2](#)
25. F. Gori, M. Santarsiero, S. Vicalvi, R. Borghi, G. Cincotti, E. Di Fabrizio, M. Gentili, Analytical derivation of the optimum triplicator. *Opt. Commun.* **157**, 13–16 (1998). [doi:10.1016/S0030-4018\(98\)00518-5](#)
26. J. Albero, J. A. Davis, D. M. Cottrell, C. E. Granger, K. R. McCormick, I. Moreno, Generalized diffractive optical elements with asymmetric harmonic response and phase control. *Appl. Opt.* **52**, 3637–3644 (2013). [Medline doi:10.1364/AO.52.003637](#)
27. A. Shaltout, J. Liu, A. Kildishev, V. Shalaev, Photonic spin Hall effect in gap–plasmon metasurfaces for on-chip chiroptical spectroscopy. *Optica* **2**, 860–863 (2015). [doi:10.1364/OPTICA.2.000860](#)
28. Y. Gorodetski, G. Biener, A. Niv, V. Kleiner, E. Hasman, Space-variant polarization manipulation for far-field polarimetry by use of subwavelength dielectric gratings. *Opt. Lett.* **30**, 2245–2247 (2005). [Medline doi:10.1364/OL.30.002245](#)
29. A. Pors, M. G. Nielsen, S. I. Bozhevolnyi, Plasmonic metagratings for simultaneous determination of Stokes parameters. *Optica* **2**, 716–723 (2015). [doi:10.1364/OPTICA.2.000716](#)
30. N. Davidson, L. Khaykovich, E. Hasman, High-resolution spectrometry for diffuse light by use of anamorphic concentration. *Opt. Lett.* **24**, 1835–1837 (1999). [Medline doi:10.1364/OL.24.001835](#)

31. A. Penzkofer, Optical rotatory dispersion measurement of D-glucose with fixed polarizer analyzer accessory in conventional spectrophotometer. *J. Anal. Sci. Methods Instrum.* **3**, 234–239 (2013).
32. K. Y. Bliokh, M. A. Alonso, E. A. Ostrovskaya, A. Aiello, Angular momenta and spin-orbit interaction of nonparaxial light in free space. *Phys. Rev. A* **82**, 063825 (2010). [doi:10.1103/PhysRevA.82.063825](https://doi.org/10.1103/PhysRevA.82.063825)
33. N. Shitrit, I. Yulevich, E. Maguid, D. Ozeri, D. Veksler, V. Kleiner, E. Hasman, Spin-optical metamaterial route to spin-controlled photonics. *Science* **340**, 724–726 (2013). [Medline doi:10.1126/science.1234892](https://doi.org/10.1126/science.1234892)
34. D. Gabor, in *Progress in Optics*, E. Wolf, Ed. (North-Holland, Amsterdam, 1961), vol. 1, pp. 109–153.
35. D. Veksler, E. Maguid, N. Shitrit, D. Ozeri, V. Kleiner, E. Hasman, Multiple wavefront shaping by metasurface based on mixed random antenna groups. *ACS Photonics* **2**, 661–667 (2015). [doi:10.1021/acsp Photonics.5b00113](https://doi.org/10.1021/acsp Photonics.5b00113)
36. Y. Yirmiyahu, A. Niv, G. Biener, V. Kleiner, E. Hasman, Vectorial vortex mode transformation for a hollow waveguide using Pancharatnam-Berry phase optical elements. *Opt. Lett.* **31**, 3252–3254 (2006). [Medline doi:10.1364/OL.31.003252](https://doi.org/10.1364/OL.31.003252)
37. R. Dorn, S. Quabis, G. Leuchs, Sharper focus for a radially polarized light beam. *Phys. Rev. Lett.* **91**, 233901 (2003). [Medline doi:10.1103/PhysRevLett.91.233901](https://doi.org/10.1103/PhysRevLett.91.233901)
38. V. Shvedov, A. R. Davoyan, C. Hnatovsky, N. Engheta, W. Krolikowski, A long-range polarization-controlled optical tractor beam. *Nat. Photonics* **8**, 846–850 (2014). [doi:10.1038/nphoton.2014.242](https://doi.org/10.1038/nphoton.2014.242)
39. R. Oron, S. Blit, N. Davidson, A. A. Friesem, Z. Bomzon, E. Hasman, The formation of laser beams with pure azimuthal or radial polarization. *Appl. Phys. Lett.* **77**, 3322–3324 (2000). [doi:10.1063/1.1327271](https://doi.org/10.1063/1.1327271)
40. S. J. Kim, P. Fan, J.-H. Kang, M. L. Brongersma, Creating semiconductor metafilms with designer absorption spectra. *Nat. Commun.* **6**, 7591 (2015). [Medline doi:10.1038/ncomms8591](https://doi.org/10.1038/ncomms8591)
41. M. Hillery, R. F. O’Connell, M. O. Scully, E. P. Wigner, Distribution functions in physics: Fundamentals. *Phys. Rep.* **106**, 121–167 (1984). [doi:10.1016/0370-1573\(84\)90160-1](https://doi.org/10.1016/0370-1573(84)90160-1)
42. J. M. R. Parrondo, J. M. Horowitz, T. Sagawa, Thermodynamics of information. *Nat. Phys.* **11**, 131–139 (2015). [doi:10.1038/nphys3230](https://doi.org/10.1038/nphys3230)
43. C. E. Shannon, A mathematical theory of communication. *Bell Syst. Tech. J.* **27**, 379–423 (1948). [doi:10.1002/j.1538-7305.1948.tb01338.x](https://doi.org/10.1002/j.1538-7305.1948.tb01338.x)
44. T. M. Cover, J. A. Thomas, in *Elements of Information Theory* (Wiley, New Jersey, ed. 2, 2006), chaps. 2, 7.